24th Australasian Fluid Mechanics Conference - AFMC2024
Canberra, Australia
1-5 December 2024

Paper No: AFMC2024-375
DOI:10.5281/zenodo.14213797

# A scalar-image based decomposition technique for cavitating flows.

**James Venning**[1*], **Elizabeth Allan**[1], **Bryce Pearce**[1], **Patrick Russell**[1],
**Luka Barbaca**[1], **and Paul A. Brandner**[1]

[1] Cavitation Research Laboratory, University of Tasmania, Launceston, Tasmania 7250, Australia
*Emailto: james.venning@utas.edu.au

## Abstract

A cross-wavelet transform (XWT) was used to elucidate the shedding modes of cavitating vortices in the wake of a nominally two-dimensional bluff body. The XWT was applied to all pixel locations in a high-speed video of the vortex street with the reference signal provided by a pressure tap in the aft-end of the bluff body. The spatial topology of the fundamental mode shape was shown to be nominally-two-dimensional spanwise vortices, though these are not linear. The spacing of the vortices was extracted. This technique allows the description of a large data set with reduced dimensionality. Calculating the modes with a relative phase instead of absolute phase allows for simpler temporal analysis.

## 1 Introduction

Data decomposition techniques are a valuable tool in the arsenal of the fluid dynamicist as they allow large, complex data sets to be described with a reduced number of dimensions. These techniques range from Fourier-based signal analysis (Welch, 1967) to the ubiquitous proper orthogonal decomposition (Lumley, 1970) or the spectral proper orthogonal decomposition (SPOD) (Schmidt, 2020; Hatzissawidis, 2024) and dynamic mode decomposition (Schmid, 2010). These techniques seek to describe the original data set with reduced dimensionality, typically decomposing data-sets into either spatio- or temporal- modes or combinations thereof. They are designed to highlight different features of the flow, for example, the POD ranks modes based on their variance, which, for a velocimetry data set, is related to the kinetic energy of each mode. Hence, a POD analysis reveals, large, energetic, often coherent flow structures.

For one-dimensional signals, the continuous wavelet transform (Torrence, 1998) provides information in the temporal-frequency space, that is, how different frequencies vary in time, see, for example Zhao (2018); Brandner (2018). The application of the CWT in fluid dynamics has been reviewed by Addison (2018). The

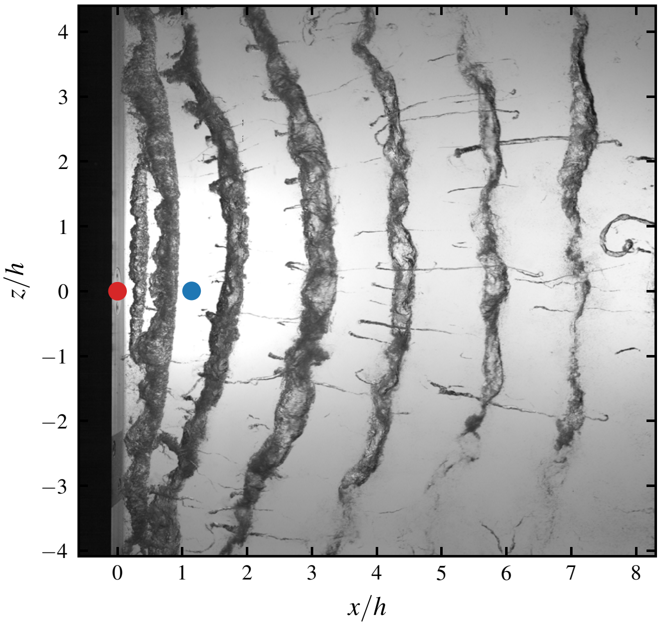

**Figure 1.** Sample photograph from the high-speed video showing the cavitating vortex street in the wake of the cylinder (left-hand side). Flow is from left to right. The blue point indicates the location of data extraction in figures 3. The red marker is the location of the pressure sensor.

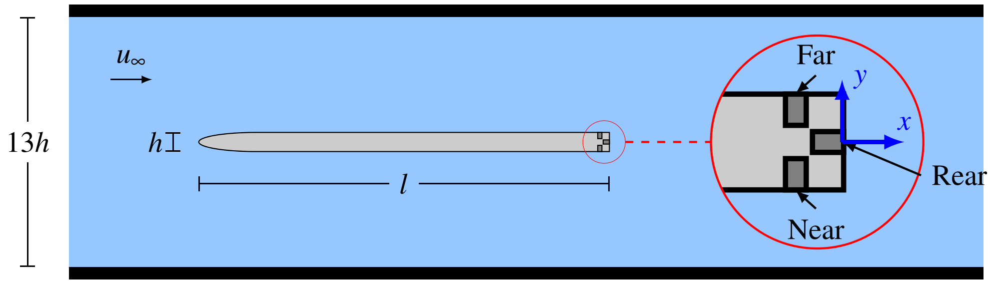

**Figure 2.** Schematic showing the square-backed elongated cylinder in the water tunnel. Key dimensions and pressure tap locations are indicated. The coordinate description is described in blue with the $z$ axis oriented out of the page.

cross-wavelet transform (Grinsted, 2004) expands this technique by comparing two CWTs from different sources, for example in Grinsted (2004) they compare the CWT of the Arctic Oscillation index with the Baltic maximum sea ice extent. The XWT reveals both the phase and coherence between the two signals of interest.

In this article, we seek to combine the methods of spatio-frequency decompositions with that of the cross-wavelet transform to identify the relationship between a 1-dimensional signal (here pressure) and a 3-dimensional signal (here high-speed video of cavitating flow). The demonstration data set is that of coherent vortex shedding behind a bluff body, acquired simultaneously with the static pressure at a location near the trailing edge. A sample video frame is provided in figure 1 showing the vortex pattern.

## 2 Experimental Setup

Experiments were conducted in the Cavitation Research Laboratory's cavitation tunnel at the University of Tasmania. The tunnel is a recirculating variable-pressure water tunnel with velocity range $2\,\mathrm{m/s}$ to $13\,\mathrm{m/s}$ and absolute pressure range $4\,\mathrm{kPa}$ to $400\,\mathrm{kPa}$. The tunnel test section is $0.6\,\mathrm{m}$ square by $2.6\,\mathrm{m}$ long and the tunnel volume is $365\,\mathrm{m}^3$ with demineralised water as the working fluid. Strict control of the nuclei population and dissolved gas levels allow continuous testing with no recirculation of gas.

A stainless steel cylinder (figure 2) with a 4:1 semi-elliptical leading edge and square trailing edge was installed on the tunnel centreline. The cylinder had height $h = 46\,\mathrm{mm}$ and length $l = 850\,\mathrm{mm}$. The cylinder fully spanned the tunnel test section and had aspect ratio (span to height) of 13. Pressure signals were acquired from three surface-mount pressure sensors (PCB 105C02) with $2.5\,\mathrm{mm}$ diameter sensing diameter located in the aft section of the cylinder. One was installed in the rear surface to measure the base pressure fluctuations (labeled 'rear'). A sensor was mounted on either side of the cylinder at a streamwise position of $x = -23\,\mathrm{mm} = -h/2$. The vertical positions were $z = -11.5\,\mathrm{mm} = -h/4$ and $z = 11.5\,\mathrm{mm} = h/4$ for the near and far sensors, respectively, where 'near' and 'far' are with respect to the camera position. For the purposes of this paper, only the 'rear' pressure sensor is analysed for the modal analysis. Pressure signals were recorded at $204.8\,\mathrm{kS/s}$ for $60\,\mathrm{s}$.

High-speed video was acquired with a Phantom v2640 camera recording images at 1000 fps with resolution 2048 px in the horizontal ($x$) direction and 1952 px in the vertical ($z$) direction. The magnification factor was $5.0\,\mathrm{px/mm}$. 50924 frames were recorded with an acquisition duration of $50.9\,\mathrm{s}$. Illumination was provided by an Effilux LED panel backlighting the images such that cavitating structures appear darker than the background.

The tunnel freestream velocity was $u_\infty = 8.33\,\mathrm{m/s}$ to achieve a length-based Reynolds number of $7 \times 10^6$. The freestream pressure was $p_\infty = 30.2\,\mathrm{kPa}$ which corresponds to a cavitation number $\sigma = \frac{p_\infty - p_v}{q} = 0.8$ with $q$ being the freestream dynamic pressure $q = \frac{1}{2}\rho u_\infty^2$. A simultaneous trigger signal was used to start both the high-speed video and the pressure acquisition.

## 3 Decomposition Technique

A sample time-series ($0.1\,\mathrm{s}$ duration) of the static pressure $p$ from the rear pressure tap is in figure 3 in light red, non-dimensionalised by the freestream dynamic pressure, $q$. The time-sequence of one pixel from the high-speed video is given in blue, located at $x/h = 1.1$ and $z/h = 0$, as indicated in figure 1 with the blue marker. This signal has been mean-removed and normalised by its standard deviation. The pressure signal is acquired at a higher rate than the high-speed video. It contains high-frequency variations (appears as spikes) due to the cavitation inception of vortices oriented in the streamwise direction (Allan, 2023). The signal is first low-pass

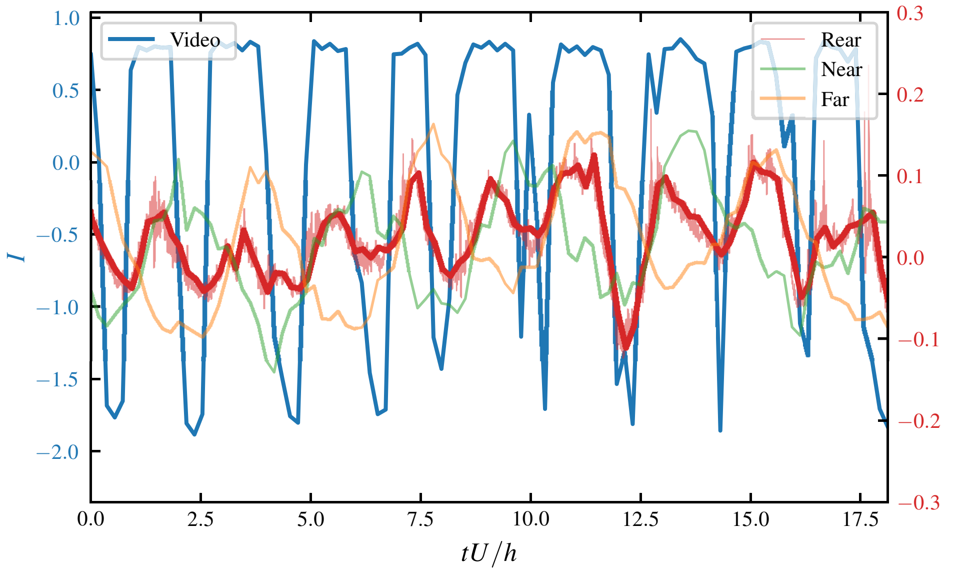

**Figure 3.** Time series of base pressure (red) and video (blue). The physical duration of this plot is 0.1 s. The blue video signal was extracted at $x/h = 1.1$ and $z/h = 0$ as indicated by the blue marker in figure 1. The near and far pressure signals are included in green and orange, respectively.

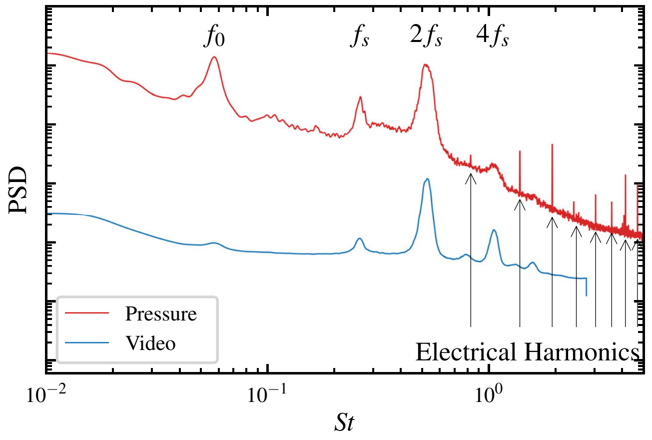

**Figure 4.** Spectra of pressure (red) and video (blue). The video spectrum is calculated by averaging the PSD of the intensity timeseries from each pixel.

filtered to remove this inception noise, and then re-sampled at the same time-base as the video. This new signal is plotted in dark red. The signals from the two other pressure taps are included for reference.

There are two noticeable frequencies of interest in this sample. The video signal reduces (darkens) about 9 or 10 times during this window, indicating the shadows of vortices at about 90 Hz to 100 Hz. The rear pressure signal has the same frequency with some phase delay. The near and far pressure signals show the shedding frequency of vortices from each side to occur about 4.5 times in this window, or with a shedding frequency of about 45 Hz. The phase between these two signals is π, indicating alternate shedding of vortices. For the rest of this paper, only the 'rear' pressure signal is used.

A Welch algorithm can be applied to the pressure timeseries (here the unfiltered) and the resultant power spectral density is given in figure 4. The fundamental shedding frequency is labeled $f_s$ and is at a Strouhal number of 0.262 or a frequency of 47 Hz. This corresponds to the dominant frequency evident in the near and far pressure signals in figure 3. The even super-harmonics of the fundamental are also evident and the first two are labeled. A low-frequency peak, labelled $f_0$ appears at a Strouhal number of 0.058 (frequency of 10.2 Hz). Electrical harmonics also appear at the odd super-harmonics of 50 Hz, with the first arrow label at 150 Hz.

The video PSD here is calculated from the spatial average of the Welch PSD applied to every pixel in the video. Unsurprisingly, the average shows many of the same peaks as the pressure signal. The dominant frequency in the video is $2f_s$ due to the passage of two vortex shadows per one pressure cycle.

The cross-wavelet algorithm (Cross wavelet and wavelet coherence software were provided by A. Grinsted (Grinsted, 2004)) was used to understand the temporal variations in the frequency content. Here, the continuous

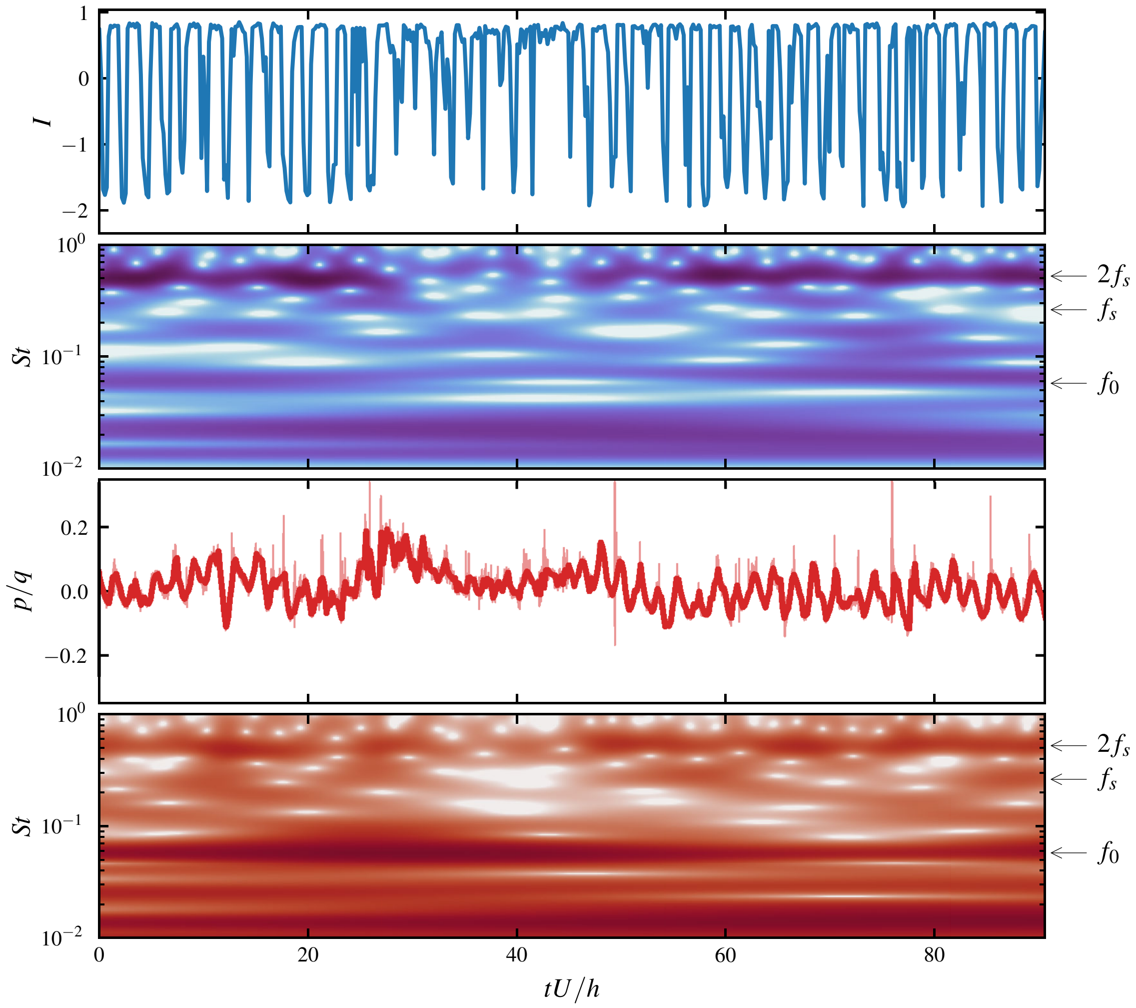

**Figure 5.** Time-series and amplitude of the continuous wavelet transform for a 0.5 s sample from the video (blue) and pressure (red) signals.

wavelet transform (CWT) with a Morlet mother is applied to each signal in turn, ie. the pressure and video signals from figure 3. The choice of mother wavelet is a compromise between frequency and temporal localisation. In this case, the Morlet wavelet provides a good compromise between the two. An example of the two signals and their corresponding CWTs are in figure 5. The filled contours represent the power of the CWT for each frequency as it varies in time. The dark blue band across much of the duration corresponds to the passing of vortices at a frequency of $2f_s$ at the probe location. This strength of this frequency breaks down for $30 < tU/h < 50$ where the video shows the vortices to be incoherent for this duration (eg. figure 6).

The CWT is used to transform each pixel in the video into a temporal-frequency map. The two complex

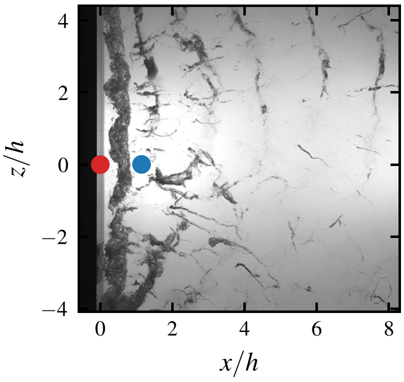

**Figure 6.** Sample photograph from the high-speed video showing the breakdown of vortex shedding. The blue point indicates the location of data extraction in figure 5. The red marker is the location of the pressure sensor.

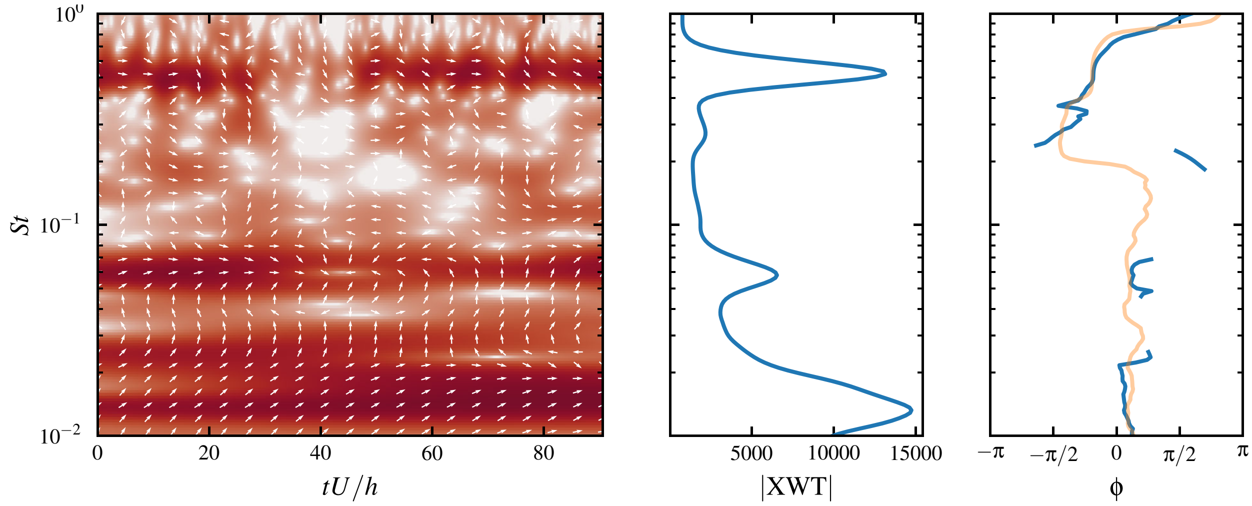

**Figure 7.** Temporal-frequency map of the absolute value of the cross-wavelet transform with arrows indicating the phase between the signals. The two signals are the samples of the video and pressure as in figure 5. Arrows indicate the phase between the signals: right is in-phase, left is out-of-phase, up is pressure leads, down is video leads. The centre panel has the time average of the coherence, and the right panel has the time averaged phase difference. Here the orange is the time-average of the phase, while the blue is averaging only portions of the time-series with high coherence.

matrices $W^p$ (CWT of the pressure signal) and $W^v$ (CWT of the video signal) are used to create the XWT $W^{pv} = W^p W^{v*}$ where $^*$ denotes the complex conjugate. The power of the XWT is the absolute value of the $W^{pv}$ and the phase angle, $\phi$ is the relative phase between $p(t)$ and $I(t)$ and is returned for all time and frequency. An example XWT is in figure 7. The filled contours are the temporal-frequency map showing the coherence between the two signals. Darker areas indicate combinations of time and frequency with common high power. The overlaid arrows on top of the map indicate the phase of the signal. Arrows to the right indicate temporal-frequency areas where the two signals are in phase. Arrows to the left are out-of-phase, arrows upward are pressure signal leading and arrows downward are pressure signal lagging by $\pi/2$. The contours in the left-panel indicate that the pressure and image (at this video location) data are coherent for much of the time-series at frequencies of $2f_s$ and $f_0$. The phase at $2f_s$ is marginally downward indicating a slight lead of the video signal. Note that the phase difference here is a function of where the video signal was extracted, that is, the video lag will increase with downstream position.

The centre panel has the time-average (of the whole 50 s signal duration) of the power of the XWT. The peaks correspond well to the results from the Welch PSD, indicating that the same frequencies of interest tend to be dominant simultaneously between the video and the pressure. The circular mean of the phase angles is the two-argument arctangent of the temporal sums of the sines and the cosines of the phase:

$$\operatorname{atan2}\left(\sum \sin(\phi_i), \sum \cos(\phi_i)\right) \tag{1}$$

This temporal-mean of the phase is given in the third panel of figure 7 which is the phase difference between the pressure and video signal. Two averages are given here. In orange is the pure time-average of $\phi$, while blue is the temporal average of only those times with high coherence between the two signals. For this location, the phase of the shedding frequency is about $-\pi/2$, so the pressure is high while a shadow of a vortex is passing this pixel.

This phase can be calculated for each pixel location in the video and for each frequency at each time. Because it is now referenced to the pressure signal, rather than an arbitrary reference (as given by a single PSD or CWT, see Venning (2021) for further discussion on decomposing spatial maps with arbitrary phase references), the phase difference can simply be plotted as a time-average across space. Such a distribution of phase reveals the spatial mode shape for each frequency. One such power and phase distribution is presented in figure 8.

The strongest mode shape shown is that of $2f_s$, which consists of a series of quasi-spanwise structures. These structures correspond to the spanwise vortical structures which dominate the video. The power of this mode is strongest near the pressure taps, due to both the higher coherence and also stronger vortices and thus higher signal variation. The spacing between lines of constant phase progresses from $0.65h$ to $1.5h$ by the end of the video field of view. This is presented in figure 9 and is indicative of the streamwise stretching between the vortices due to the merging of the two shear layers.

In the spanwise direction, the modes are quasi-parallel, but by no means perfectly so, indicating that the

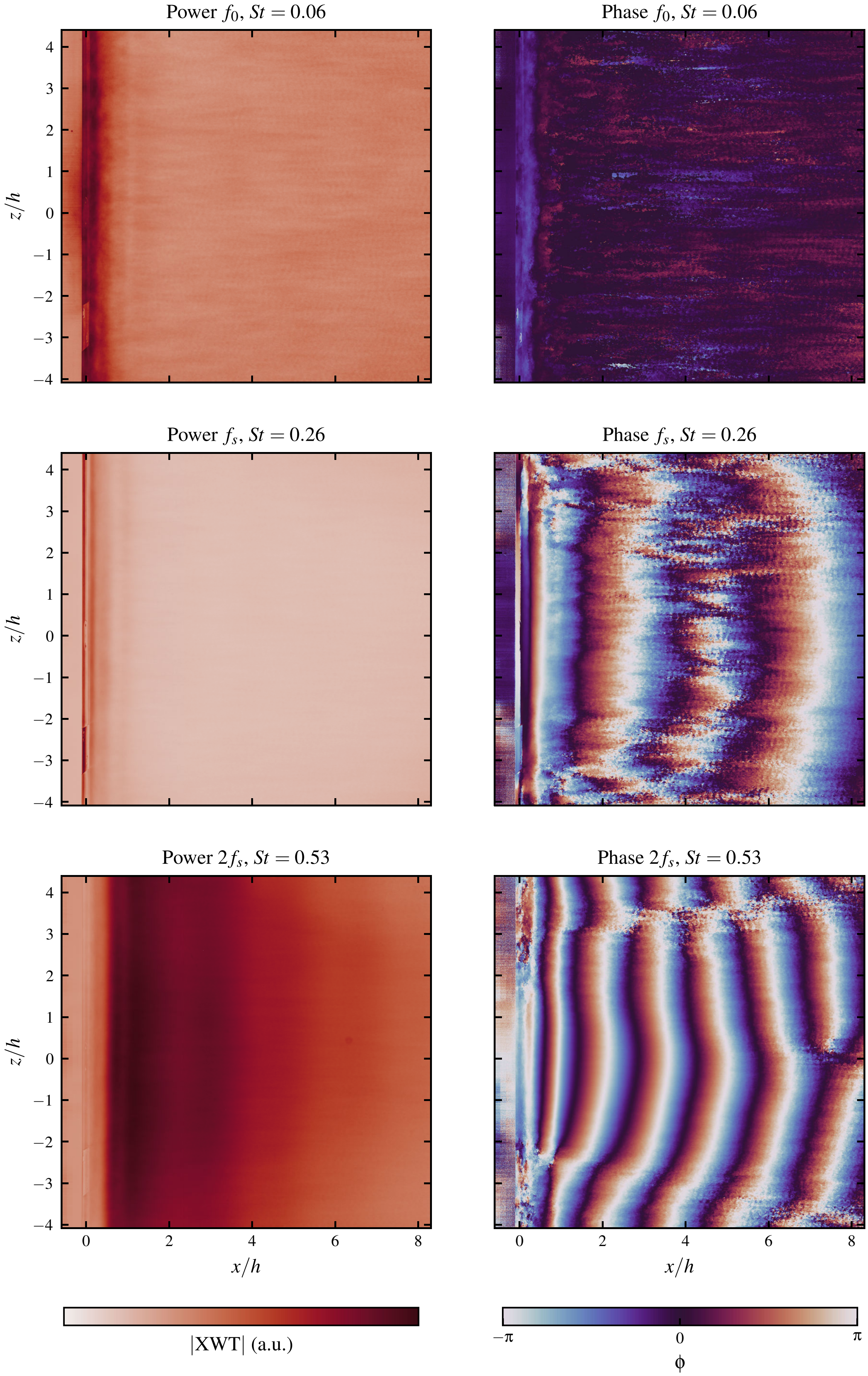

**Figure 8.** Mode amplitudes (left) and phase difference (right) for the three frequencies of interest.

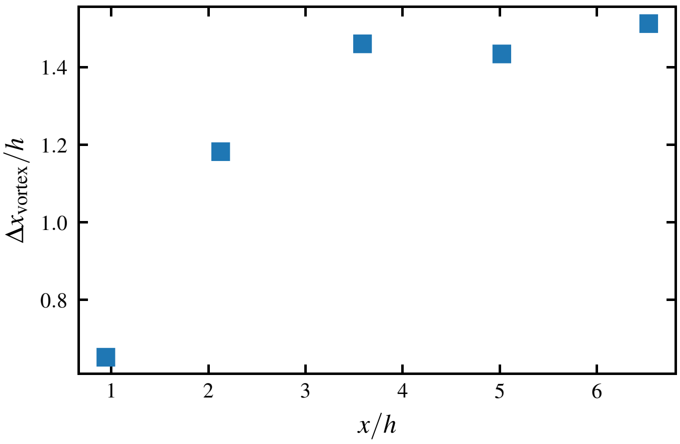

**Figure 9.** Spacing between lines of equal phase difference as the vortex street develops downstream.

vortices tend to not be perfectly parallel. This can be seen in the example frame shown in figure 1. Such a result indicates that the spanwise aspect ratio (13) is insufficient to ensure two-dimensional shedding. This perhaps could be achieved with a larger cylinder or end-conditioning. Care would need to be taken regarding the effect of hydrostatic pressure difference on the cavitation. Another interesting phenomenon is the phase discontinuity that appears near $z/h \pm 2.5$, expanding with the downstream direction.

Unfortunately, little can be gleaned from the $f_0$ mode ($f = 10\,\mathrm{Hz}$, $St = 0.06$). The mode is evident in both the video and pressure signals. The phase between the video and pressure signal is near $-\pi/4$ along the rear edge of the cylinder, where the mode has energy. Given the mode is fairly uniform across the $xz$ plane, out-of-plane vibration is a possible explanation, or some manifestation of a tunnel instability such as surge. Future experiments could utilise a displacement or acceleration measurement to determine this.

## 4 Conclusions

A decomposition technique has been described combining data from a spatio-temporal map (in this case high-speed video of a cavitating vortex system) with a scalar time-series (in this case a pressure signal). The use of wavelets is advantageous as it gives insights into the temporal nature of modes of interest, such as periods of vortex breakdown. By referencing the wavelets to a common pressure signal, the phase difference was obtained, rather than solely the phase as is typically obtained from spectral methods. Spatial maps of this phase difference show the dominant mode to be that of the coherent shedding of nominally two-dimensional spanwise vortices, however, the maps also indicate the strong presence of spanwise variation in the phase, ie. the vortices tend to not be parallel for the entire domain.

## Acknowledgments

The authors acknowledge the support of Defence Science Technology Group (DST) and the technical support of Robert Wrigley and Steven Kent.

## References

Addison, P. S. 2018. Introduction to redundancy rules: the continuous wavelet transform comes of age. *Philosophical Transactions of the Royal Society A: Mathematical, Physical and Engineering Sciences*, 376(2126), 20170258.

Allan, E. S. C., Barbaca, L., Venning, J. A., Russell, P. S., Pearce, B. W., and Brandner, P. A. (2023). Nucleation and cavitation inception in high Reynolds number shear layers. *Physics of Fluids*, 35(1).

Brandner, P. A., Venning, J. A., and Pearce, B. W. 2018. Wavelet analysis techniques in cavitating flows. *Philosophical Transactions of the Royal Society A: Mathematical, Physical and Engineering Sciences*, 376(2126), 20170242.

Grinsted, A., J. C. Moore, S. Jevrejeva 2004, Application of the cross wavelet transform and wavelet coherence to geophysical time series, *Nonlin. Process. Geophys.*, **11**, 561566.

Hatzissawidis, G., Sieber, M., Oberleithner, K., Pelz, P. 2004, Data-driven spatiotemporal analysis of cloud cavitation by means of Spectral Proper Orthogonal Decomposition, Under consideration for publication in *Exp. Fluids*.

Lumley, J. L. 1970, Stochastic Tools in Turbulence *Academic Press*

Schmid, P. J. 2010, Dynamic mode decomposition of numerical and experimental data. *Journal of Fluid Mechanics*, 656, 5-28.

Schmidt, O. T., and Colonius, T. 2020, Guide to spectral proper orthogonal decomposition. *AIAA journal*, 58(3), 1023-1033.

Torrence, C., and Compo, G. P. 1998. A practical guide to wavelet analysis. *Bulletin of the American Meteorological society*, 79(1), 61-78.

Venning, J. A., Pearce, B. W., and Brandner, P. A. 2021. Dual-camera mode visualization of cavitating flows. *In 11th International Symposium on Cavitation–CAV2021.*

Welch, P. 1967, The use of fast Fourier transform for the estimation of power spectra: a method based on time averaging over short, modified periodograms, *IEEE Transactions on audio and electroacoustics*, **15(2)**, 70-73.

Zhao, J., Nemes, A., Lo Jacono, D., and Sheridan, J. 2018. Branch/mode competition in the flow-induced vibration of a square cylinder. *Philosophical Transactions of the Royal Society A: Mathematical, Physical and Engineering Sciences*, 376(2126), 20170243.